Temperature dependence of spectral and laser properties of Er^{3+}/Al^{3+} co-doped aluminosilicate fiber

Qiang He (何 强)[1,2], Fan Wang (王 璠)[1,2], Zhiquan Lin (林治全)[1,2], Chongyun Shao (邵冲云)[1,2], Meng Wang (王 孟)[1], Shikai Wang (王世凯)[1], Chunlei Yu (于春雷)[1,*], and Lili Hu (胡丽丽)[1]

[1]*Shanghai Institute of Optics and Fine Mechanics, Chinese Academy of Sciences, Shanghai 201800, China*
[2]*Center of Materials Science and Optoelectronics Engineering, University of Chinese Academy of Sciences, Beijing 100049, China*
**Corresponding author: sdycllcy@siom.ac.cn*

Received May 10, 2019; accepted July 26, 2019; posted online August 27, 2019

Using a heavily erbium-doped aluminosilicate fiber prepared by the sol-gel method combined with high temperature sintering, the temperature dependence of the spectrum around the 1.55 nm band and single-mode fiber laser properties were investigated, respectively. The absorption cross section increases 29.2% at ~1558 nm with the temperature increasing from 20°C to 140°C, while the emission cross section slightly increases 4.3%. In addition, the laser slope of the heavily erbium-doped aluminosilicate fiber at 1558 nm decreases 4.4% from 10.8% to 6.4% with the temperature increasing from 18°C to 440°C. Meanwhile, an experiment lasting 3 h proves that the fiber laser has excellent stability below 440°C.

OCIS codes: 140.3500, 060.2400, 120.6810, 140.3425.
doi: 10.3788/COL201917.101401.

Erbium-doped fiber lasers (EDFLs) and erbium-doped fiber amplifiers (EDFAs) have been widely used in supercontinuum sources, remote sensing, and light detection and ranging (LIDAR)[1–4]. High peak power and pulse energy are required for many applications, such as coherent Doppler LIDAR, for long range wind sensing[5,6]. In the condition of high pumped power, heat is generated into the active medium (fiber core) because of a quantum defect between the pump and laser photons[7]. In spite of the large dissipation power of fibers, the fiber core temperature can reach several hundred degrees of centigrade, as well as the thermal effects starting to be significant in fiber lasers[8]. Thus, the performance of erbium-doped fibers (EDFs) under high power pumping becomes one of the research focuses. On the one hand, several amazing approaches are applied to meet the requirements of high output power of EDFLs. First, by energy transferring from $Yb^{3+}(^2F_{5/2})$ to $Er^{3+}(^4I_{11/2})$, Er^{3+}/Yb^{3+} co-doped fibers can achieve high power near 1.55 μm due to the high absorption cross section of Yb^{3+} at 976 nm[9,10]. However, the parasitic Yb^{3+} lasing at ~1 μm with a high thermal load under high power pumping is detrimental for power scaling or high gain[11–13]. Then, another approach that uses Yb^{3+}-free heavily EDFs can avoid the parasitic fluorescence of Yb^{3+}[14,15], which can also reduce the fiber length effectively and the nonlinear effects due to high power[11]. On the other hand, some reports have confirmed that optical gain of EDFs changes with high temperature[16], which is attributed to the high temperature dependence of the rare earth (RE) ion properties. Meanwhile, theoretical algorithms and numerical simulations are applied frequently to predict and optimize the performance of EDFLs or EDFAs[17]. However, an increasing error between simulations and experiments occurs due to the lack of the representability of the spectroscopic parameters used in these numerical simulations[18,19]. Therefore, an increasing requirement of parameters of the spectrum and laser occurs in these simulations.

In this work, we studied the temperature dependence of absorption/emission cross sections of heavily Er-doped aluminosilicate glass ranging from 20°C to 140°C. Using the Yb^{3+}-free heavily Er^{3+}/Al^{3+} co-doped fiber (EADF), we investigated the experimental evolution of laser properties with temperatures ranging from 20°C to 440°C. Finally, the stability of output power of the fiber laser was experimentally investigated at high temperature.

Figure 1 shows the energy level diagram of Er^{3+} in aluminosilicate[20,21]. The upper energy level $^4I_{13/2}$ and ground energy level $^4I_{15/2}$ split into seven sublevels and

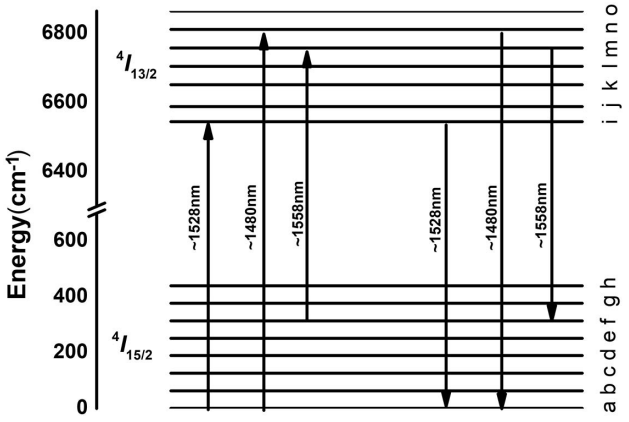

Fig. 1. Diagram of Stark splitting of $^4I_{13/2}$ and $^4I_{15/2}$ of Er^{3+} in aluminosilicate glass.

eight sublevels, respectively, due to $Er^{3+} - Er^{3+}$ interaction with the surrounding host.

A high concentration of Er^{3+} easily forms clusters in the preparation process of Er^{3+}-doped fiber, which will seriously affect the laser performance[22,23]. The insertion of Al^{3+} ions is beneficial to homogenize the distribution of Er^{3+} ions in aluminosilicate glass[24]. In this work, the Er/Al co-doped core glass (with an Er/Al ratio of ~10) was prepared by the sol-gel method combined with high temperature sintering. Finally, a silica preform was prepared by the rod-in-tube method, and a double cladding Er^{3+}/Al^{3+} co-doped silica fiber was drawn. The core and inner cladding diameters are 8 μm and 100 μm, respectively. The numerical aperture (NA) is ~0.15. Meanwhile, the distribution of Er^{3+} ions in core glass turns out to be homogenous, and the clusters of Er^{3+} were well suppressed[24]. The concentration of Er^{3+} reaches 1.19×10^{20} ions/cm^3, measured by inductively coupled plasma optical emission spectrometry (ICP-OES).

An obvious self-absorption near the zero phonon line (~1528 nm) can occur due to high concentrations of Er^{3+}, which can reduce fluorescence lifetime between $^4I_{15/2}$ and $^4I_{13/2}$[25]. In this work, a treatment is used to avoid the effect of self-absorption by using a 0.5-mm-thick slice cut from the core glass and polished for all spectroscopic measurements. The fluorescence lifetime of the sample at different temperatures is measured by the time-resolved spectrometer (Edinburgh Instruments, FLS920) pumped with a pulsed 980 nm diode laser. The slice was pressed against a copper plate and heated by heat conduction from 20°C to 140°C with 40°C steps (10 min stabilization time).

The temperature dependence of the fluorescence lifetime of $^4I_{13/2}$ is shown in Fig. 2. The fluorescence lifetime decreases 0.42 ms gradually as temperature increases. Fluorescence lifetime is a quantity in which all of the possible de-excitation processes are reflected, being strongly sensitive to the radiation trapping effects (known as self-absorption) and amplified spontaneous emission (ASE)[26]. Self-absorption and ASE can be neglected by using a thin sample. Thus, the de-excitation process of the upper energy level $^4I_{13/2}$ to ground energy level $^4I_{15/2}$ can be reflected by the fluorescence lifetime approximately. The de-excitation process of the upper energy level $^4I_{13/2}$ includes radiative transition and phonon-assisted transition (nonradiative transition). It can be considered that the radiation transition is almost irrespective of temperature due to the energy gap (6540 cm^{-1}) that is much larger than kiloteslas (kT) (~500 cm^{-1}). Therefore, the decreases of fluorescence lifetime can lead to the intensifying of nonradiative transition. This result indicates that the nonradiative transition process with phonon assistance is more significant with the increase of temperature.

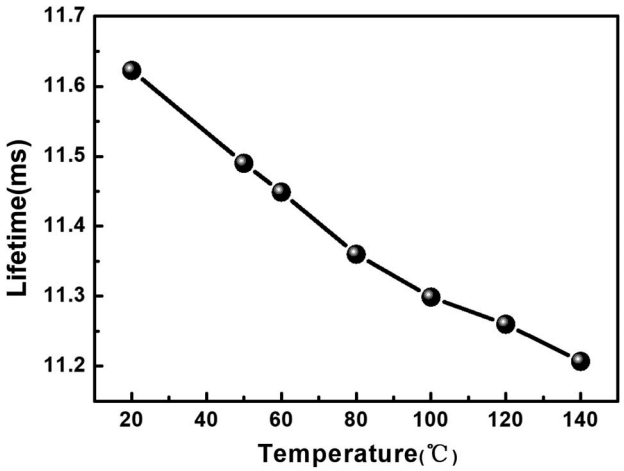

Fig. 2. Evolution of fluorescence lifetime of energy level $^4I_{13/2}$ with temperature in Er^{3+}:aluminosilicate glass.

Temperature can affect the occupation distribution of the involved Stark levels and the transition probability of the stimulated ions, which can exhibit spectroscopically as a change of the absorption and emission cross section with temperature. The absorption spectrum was measured by a Lambda 950 UV-visible-near-IR (UV-VIS-NIR) spectrophotometer. Similarly, the thin sample was heated by a perforated copper block, which can allow the pump light to pass through. The absorption cross sections $\sigma_a(\lambda, T)$ of Er^{3+} can be calculated by Lambert–Beer's law[27]:

$$\sigma_a(\lambda, T) = \frac{\ln[I_0(\lambda, T)/I_{out}(\lambda, T)]}{N_{dot} l}, \tag{1}$$

where N_{dot} is the concentration of Er^{3+} in the sample, and l is the thickness of the sample. The reference intensity $I_0(\lambda, T)$ and the transmitted intensity $I_{out}(\lambda, T)$ are measured with the white light beam. Considering the Fresnel reflection on the surface of the sample, they are both normalized in the regions from 850 nm to 900 nm and from 1650 nm to 1700 nm, where absorption can be ignored.

Figure 3 shows the absorption cross sections in Er^{3+}:aluminosilicate glass at different temperatures. The absorption cross sections near the zero phonon line decrease 13.3% from 0.525×10^{-20} cm^2 to 0.47×10^{-20} cm^2, as temperature increases from 20°C to 140°C. In addition, the absorption cross sections at two general pump wavelengths (~980 nm and ~1480 nm) also decrease significantly to 12.2% and 14%, respectively. It is worth noticing that the absorption cross section at 1558 nm increases 29.2%, which leads to more serious self-absorption near 1560 nm in Er^{3+} doped optical fiber at higher temperatures.

The McCumber theory has proven to be an available way to obtain the emission cross section from absorption cross section at different temperatures[22]. We can obtain the emission cross section $\sigma_e(\lambda, T)$ of Er^{3+} by using the following relation[28,29]:

$$\sigma_e(\lambda, T) = \sigma_a(\lambda, T) \exp\left(\frac{\epsilon - hc/\lambda}{kT}\right), \tag{2}$$

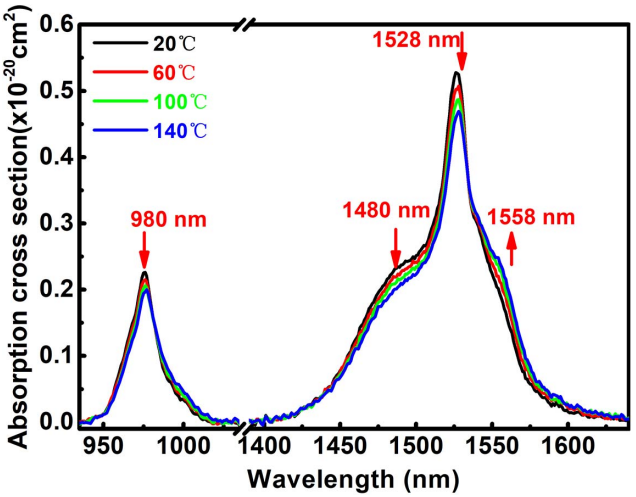

Fig. 3. Absorption cross sections in Er^{3+}:aluminosilicate glass at different temperatures.

where h, k, and c are the Planck constant, Boltzmann constant, and light speed in vacuum, respectively, and $\sigma_a(\lambda, T)$ is the absorption cross section at temperature T. The temperature-dependent excitation energy ϵ at temperature T can be calculated from the expression[30]

$$\epsilon(T) = \Delta E_0 + kT \ln\left[\frac{1+\sum_{j=2}^{8}\exp(-\Delta E_{2j}/kT)}{1+\sum_{i=2}^{7}\exp(-\Delta E_{1i}/kT)}\right], \quad (3)$$

where ΔE_0 is the separation between the lowest sublevel of each manifold, and ΔE_{1i} (ΔE_{2j}) is the energy difference between the ith (jth) sublevel and the lowest sublevel in the upper (lower) manifold.

Figure 4 shows the emission cross sections of Er^{3+}-doped aluminosilicate glass versus temperature, which can be calculated from Eq. (2). With the increase of temperature from 20°C to 140°C, it can be found that the emission cross section slightly decreases 4.3% at 1528 nm, while the emission cross section slightly increases 12.5% at 1558 nm.

The change of the absorption cross section and emission cross section with temperature can be attributed to the change of the population of distribution on Stark sublevels with temperature. In thermal equilibrium disturbance, the population of Stark sublevels of Er ions follows Boltzmann's law[31]:

$$N_i/N = \frac{\exp(-E_i/kT)}{\sum_i \exp(-E_i/kT)}, \quad (4)$$

where N_i is the number of particles of the ith sublevel in the manifold, and N is the total number of particles in the manifold. E_i is the energy of ith sublevel in each manifold at temperature T, and k is the Boltzmann constant. Figure 5 shows the normalized particle population of some sublevels in Fig. 1 as a function of temperature. In Fig. 1, the narrow 1528 nm absorption line corresponds to the transition from sublevel a to i. The ~1480 nm absorption band corresponds to the transition from sublevels a to n and m, while the ~1558 nm absorption band corresponds to the transition from sublevel m to g. As shown in Fig. 5, with the increase of temperature, the particle population of sublevel a in $^4I_{15/2}$ decreases, which leads to the decreasing of the absorption cross section at 1528 nm and 1480 nm. However, an increasing of sublevel g leads to the increasing of the absorption cross section at 1558 nm. Similar to the absorption cross section, the population decrease of the lowest sublevel i in the $^4I_{13/2}$ leads to a decreasing of the emission cross section at 1528 nm. Inversely, higher sublevels m and n have larger populations with the increase of temperature, which leads to the increasing of the emission cross section at 1558 nm and 1480 nm.

An all-fiber laser cavity was built with a heating device, as shown in Fig. 6. Two fiber Bragg gratings (FBGs) with a peak reflection wavelength at 1558 nm were used. The reflection coefficients of FBGs are 49% and 99%,

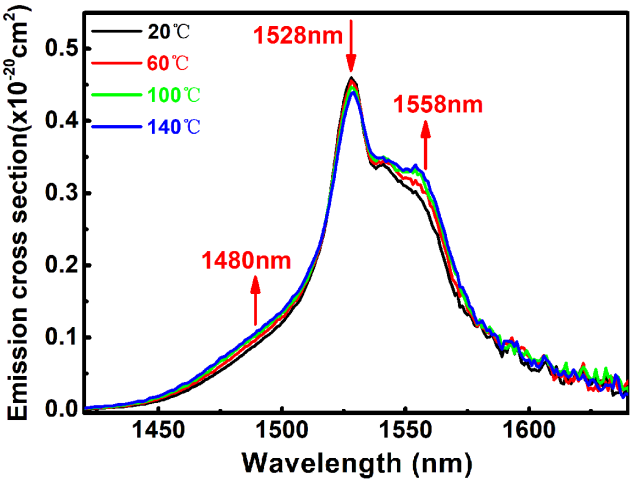

Fig. 4. Emission cross sections in Er^{3+}:aluminosilicate glass at different temperatures.

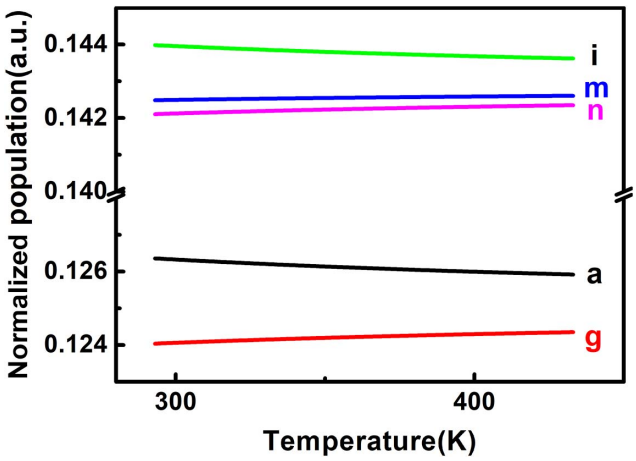

Fig. 5. Evolution of normalized population of Stark sublevels in manifolds $^4I_{13/2}$ and $^4I_{15/2}$ with temperature.

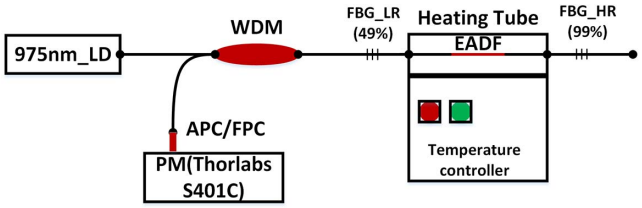

Fig. 6. Schematic diagram of all-fiber experiment setup.

respectively. Meanwhile, two FBGs were placed outside the heating tube due to the temperature sensitivity of the FBG, such as reflectivity and wavelength[32]. The EADF was fused to a single-mode fiber (SMF-28) and core pumped by a single-mode laser diode (LD) operating at 975 nm. An angled physical contact/fiber patch cord (APC/FPC) port was connected to photosensitive optical power meter (PM, Thorlabs S401C). An 8.7-cm-long double cladding EADF was placed into the middle part of the heating tube, which has a uniform distribution of temperature.

As shown in Fig. 7, the laser output power versus pump power was measured, ranging from 18°C to 440°C with 70°C steps. It can be seen that the output power decreases 54% from 14 mW to 6.5 mW with 180 mW pump power. From the evolution of absorption cross sections ranging from 920 nm to 1030 nm in Fig. 3, absorption cross sections at 976 nm decreased from 0.226×10^{-20} cm^2 to 0.198×10^{-20} cm^2 with the temperature increasing from 20°C to 140°C. Thus, the absorption coefficient of the EADF at the pump wavelength decreased 3.4 m^{-1} from 26.9 m^{-1} to 23.5 m^{-1}, according to the relationship between the absorption cross section $\sigma_a(\lambda, T)$ and the absorption coefficient $\delta(\lambda, T)$,

$$\delta(\lambda, T) = N_{Er} \times \sigma_a(\lambda, T), \tag{5}$$

where N_{Er} is the concentration of Er^{3+} in the optical fiber. The absorbed pump power of fiber with a fixed length decreases with the increase of temperature. Then, the output laser power and the slope efficiency decrease when the fiber temperature increases. The decreasing of the output power means a decreasing of slope efficiency with the same pump power. The slope efficiency decreases 4.4% from 10.8% to 6.4%, as shown in Fig. 8.

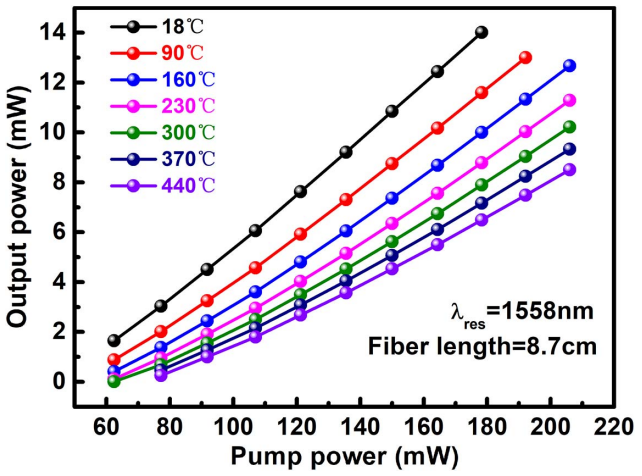

Fig. 7. Measured output power versus different temperatures.

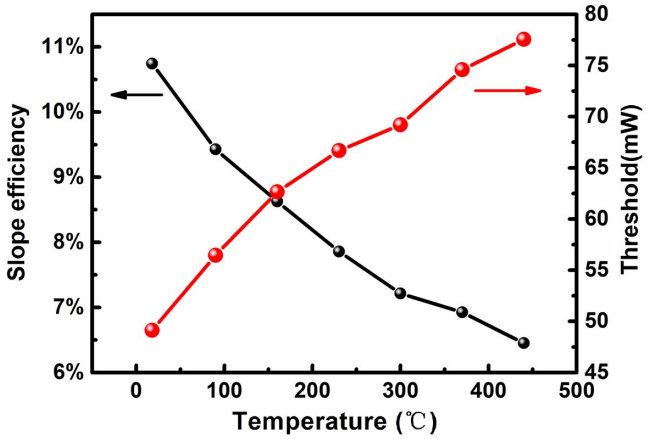

Fig. 8. Temperature dependence of slope efficiency and laser threshold.

In order to deeply analyze the effect of temperature on EADF, the evolution of the threshold of pump power with temperature is depicted in Fig. 8. As the temperature increases from 20°C to 440 °C, the threshold pump power increases 60% from 48 mW to 77 mW. The threshold pump power of the fiber laser is the result of the balance of signal light gain and loss in the resonator cavity. With the increase of temperature, the gain decreases approximately linearly in spite of the increasing in the emission cross section[33]. According to Eq. (5), the loss coefficient of EADF increases from 20.63 m^{-1} to 26.45 m^{-1} due to the increasing of the absorption cross section at 1558 nm. The gain of signal light increases with 975 nm pump power before the gain reaches saturation. A steady resonator cavity needs an increasing pump power, which results in an increasing threshold pump power with increasing temperature. Indeed the energy level lifetime of $^4I_{15/2}$ decreased sharply with an increasing temperature. The phonon-assisted nonradiative relaxation intensifies in the resonator cavity, resulting in the decreasing number of inverted particles between $^4I_{15/2}$ and $^4I_{13/2}$. A sufficiently large number of inverted particles can only be formed by pumping particles faster from ground level $^4I_{15/2}$ to the upper level $^4I_{9/2}$, which results in an increase of threshold pump power.

The stability of laser output power under high temperature conditions is very important in laser applications. In order to investigate the stability of the fiber laser at high temperatures, the EADF was heated at different given temperatures, and the output laser power was recorded ceaselessly. The temperature curve was set to a ladder, as shown in Fig. 9. It can be seen that the output power of the laser has excellent stability, especially under the condition of 440°C in 3 h, where the output power fluctuates within 1.03%.

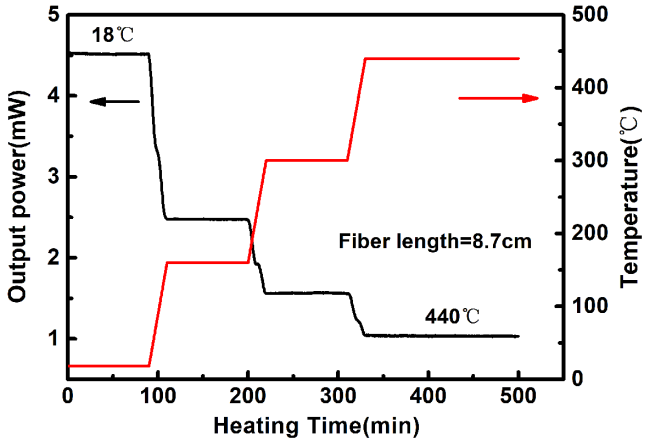

Fig. 9. Evolution of output power and temperature with heating time.

In conclusion, a heavily Er^{3+}/Al^{3+} co-doped aluminosilicate glass fiber was prepared. The temperature dependences of the absorption cross sections, emission cross sections, and fluorescence lifetime are investigated. As temperature increases from 20°C to 140°C, the absorption section of Er^{3+} decreases 13.4% at 1528 nm and increases 29.3% at 1558 nm. Meanwhile, the emission section decreases by 4.3% at 1528 nm and 12.5% at 1558 nm, respectively. Then, the temperature dependence of laser output power (pumped at 975 nm and lased at 1558 nm) was measured, ranging from 20°C to 440°C through a 8.7-cm-long EADF. The laser output power reduces 50% from 13 mW to 6.5 mW with 180 mW pump power due to the decrease of the absorption cross section near the pump wavelength. Meanwhile, the laser efficiency decreases 4.4%, from 10.8% to 6.4%. The threshold pump power increases 60% due to the decreasing fluorescence lifetime at ~1558 nm. The stability of the laser output power at different high temperatures is also studied, and the laser output shows a high stability at our experimental temperature.

This work was financially supported by the National Natural Science Foundation of China (NSFC) (No. 61775224).

References

1. M. Lopez-Ripa, S. Jarabo, and F. J. Salgado-Remacha, Opt. Lett. **44**, 2016 (2019).
2. S. Cai, Z. Zhang, and X. Chen, Opt. Commun. **439**, 164 (2019).
3. E. Gregorio, X. Torrent, S. Planas, F. Solanelles, R. Sanz, F. Rocadenbosch, J. Masip, M. Ribes-Dasi, and J. R. Rosell-Polo, Sensors **16**, 499 (2016).
4. S. Diaz, J. Lightw. Technol. **34**, 4591 (2016).
5. X. B. Rui, P. Guo, H. Chen, S. Y. Chen, Y. C. Zhang, M. Zhao, Y. W. Wu, and P. T. Zhao, Opt. Eng. **58**, 034105 (2019).
6. S. Wu, X. H. Zhai, and B. Y. Liu, Opt. Express **27**, 1142 (2019).
7. T. Yao, J. Ji, and J. Nilsson, J. Lightw. Technol. **32**, 429 (2014).
8. Y. Y. Fan, B. He, J. Zhou, J. T. Zheng, H. K. Liu, Y. R. Wei, J. X. Dong, and Q. H. Lou, Opt. Express **19**, 15162 (2011).
9. J. Nilsson, S. Alam, J. A. Alvarez-Chavez, P. W. Turner, W. A. Clarkson, and A. B. Grudinin, IEEE J. Quantum Electron. **39**, 987 (2003).
10. Y. Jeong, S. Yoo, C. A. Codemard, J. Nilsson, J. K. Sahu, D. N. Payne, R. Horley, P. W. Turner, L. Hickey, A. Harker, M. Lovelady, and A. Piper, IEEE J. Sel. Top. Quant. **13**, 573 (2007).
11. K. Tankala, B. Samson, A. Carter, J. Farroni, D. Machewirth, N. Jacobson, U. Manyam, A. Sanchez, M. Y. Cheng,, A. Galvanauskas, W. Torruellas, and Y. Chen, Proc. SPIE **6102**, 610206 (2006).
12. V. Kuhn, P. Webels, J. Neumann, and D. Kracht, Opt. Express **17**, 18304 (2009).
13. G. Canat, J.-C. Mollier, Y. Jaouën, and B. Dussardier, Opt. Lett. **30**, 3030 (2005).
14. L. V. Kotov, M. M. Bubnov, D. S. Lipatov, A. N. Guryanov, S. Fevrier, J. Lhermite, E. Cormier, M. Y. Koptev, E. A. Anashkina, S. V. Muraviev, A. V. Andrianov, A. V. Kim, and M. E. Likhachev, Proc. SPIE **8961**, 89611L (2014).
15. C. C. Baker, E. J. Friebele, C. G. Askins, M. P. Hunt, B. A. Marcheschi, J. Fontana, J. R. Peele, W. Kim, J. Sanghera, J. Zhang, R. K. Pattnaik, L. D. Merkle, M. Dubinskii, Y. Chen, I. A. Dajani, and C. Mart, Proc. SPIE **9728**, 97280T (2016).
16. N. Kagi, A. Oyobe, and K. Nakamura, J. Lightw. Technol. **9**, 261 (1991).
17. A. Giaquinto, L. Mescia, G. Fornarelli, and F. Prudenzano, Opt. Lett. **36**, 142 (2011).
18. R. S. Quimby, J. Appl. Phys. **92**, 180 (2002).
19. R. M. Martin and R. S. Quimby, J. Opt. Soc. Am. B. **23**, 1770 (2006).
20. E. Desurvire and J. R. Simpon, Opt. Lett. **15**, 547 (1990).
21. M. J. F. Digonnet, E. Murphy-Chutorian, and D. G. Falquier, IEEE J. Quantum Electron. **38**, 1629 (2002).
22. I. Savelii, L. Bigot, B. Capoen, C. Gonnet, C. Chanéac, E. Burova, A. Pastouret, H. El-Hamzaoui, and M. Bouazaoui, Nanoscale Res. Lett. **12**, 206 (2017).
23. M. Z. Amin and K. K. Qureshi, Chin. Opt. Lett. **15**, 010601 (2017).
24. F. Wang, Z. Q. Lin, C. Y. Shao, Q. L. Zhou, L. Zhang, M. Wang, D. P. Chen, G. J. Gao, S. K. Wang, C. L. Yu, and L. L. Hu, Opt. Lett. **43**, 2356 (2018).
25. W. L. Barnes, R. I. Laming, E. J. Tarbox, and P. R. Morkel, IEEE J. Quantum Electron. **27**, 1004 (1991).
26. P. L. Pernas and E. Cantelar, Physica Scripta. **T118**, 93 (2005).
27. J. Koerner, C. Vorholt, H. Liebetrau, M. Kahle, D. Kloepfel, R. Seifert, J. Hein, and M. C. Kaluza, J. Opt. Soc. Am. B. **29**, 2493 (2012).
28. A. Ladaci, S. Girard, L. Mescia, T. Robin, B. Cadier, A. Laurent, M. Boutillier, B. Sane, E. Marin, Y. Ouerdane, and A. Boukenter, IEEE J. Quantum Electron. **54**, 7000207 (2018).
29. S. Q. Xu, Z. M. Yang, S. X. Dai, J. J. Zhang, L. L. Hu, and Z. H. Jiang, J. Rare Earth **22**, 3 (2004).
30. W. J. Miniscalco and R. S. Quimby, Opt. Lett. **16**, 258 (1991).
31. D. A. Grukh, A. S. Kurkov, V. M. Paramonov, and E. M. Dianov, Quantum Electron. **34**, 579 (2004).
32. H. Li, Q. C. Zhao, S. D. Jiang, J. S. Ni, and C. Wang, Chin. Opt. Lett. **17**, 040603 (2019).
33. J. A. Bebawi, I. Kandas, M. A. El-Osairy, and M. H. Aly, Appl. Sci. **8**, 1640 (2018).